

Néel domain walls with bistable chirality in a perpendicularly magnetized ferrimagnetic insulator

Received: 6 September 2024

Accepted: 22 May 2025

Published online: 04 June 2025

Yixuan Song^{1,3}, Siying Huang^{1,3}, David Bono¹, Jerzy T. Sadowski²,
Caroline A. Ross¹✉ & Geoffrey S. D. Beach¹✉

Field-free spin-orbit torque-driven domain wall motion in magnetic thin films with perpendicular magnetic anisotropy (PMA) requires the domain walls to have Néel character. Conventionally, Néel domain walls are stabilized by the Dzyaloshinskii-Moriya interaction (DMI) in ultrathin films. Here, in a europium iron garnet thin film with PMA and an additional uniaxial in-plane anisotropy, we demonstrate two bistable Néel domain wall states in the absence of DMI, and the capability to toggle the wall states with an in-plane field pulse and consequently their directions of motion under a current pulse. We present a phase diagram for the bistable Néel domain wall states as a function of in-plane field pulse width and amplitude. By fitting the experimental data to an analytical model of Néel wall reversal through the nucleation and propagation of Bloch lines, we extract the length of the initial reversed domain wall segment and Bloch line nucleation energy barrier. Current-driven motion of in-plane anisotropy stabilized Néel walls is qualitatively different from that of DMI-stabilized ones owing to the different symmetry of the effective fields that stabilize the Néel configuration. Furthermore, we present a proof of principle demonstration for 2-bit random number generation based on the stochastic reversal of domain wall chirality. These results provide critical insight into the topological energy barrier of Bloch lines and identify paths towards domain wall-based memory and computing devices.

Current-driven domain wall (DW) dynamics in magnetic thin films with perpendicular magnetic anisotropy (PMA) is of great interest for spintronic logic and memory applications, including racetrack memory^{1,2}. The most efficient means of current-driven DW displacement is through spin-orbit torque (SOT), in which a spin current is injected from a heavy metal layer in contact with the magnetic film. SOT-driven DW motion can be well understood in the framework of the one-dimensional model^{3–8} which describes the DW structure with a single angular variable that spans the whole wall volume: the in-plane (IP) orientation of local magnetization, in other words, the Néel

component of the wall. The SOT-driven velocity is proportional to this Néel component, which is usually stabilized by an interfacial DMI (iDMI)^{5,7–9}, and the direction of the DW motion is set by the DW chirality, which is fixed in materials with strong iDMI. A practical scheme for stabilizing degenerate Néel DWs of either chirality in the remanent state, and for fast and reliable switching of the chirality on demand, has been lacking. While gate control of DW chirality by changing the sign of iDMI has been demonstrated¹⁰, challenges that exist include long gating times, volatility of the gated state, and the irreversible modification of the energy landscape upon gating.

¹Department of Materials Science and Engineering, Massachusetts Institute of Technology, Cambridge, MA 02139, USA. ²Center for Functional Nanomaterials, Brookhaven National Laboratory, Upton, NY 11973-5000, USA. ³These authors contributed equally: Yixuan Song, Siying Huang. ✉e-mail: caross@mit.edu; gbeach@mit.edu

Here, we present a (110)-oriented EuG thin film with PMA, which exhibits a novel field-free SOT-driven DW motion resulting from stabilization of the Néel component of the DW. The film, while OOP magnetized, has a strong IP uniaxial anisotropy, and the Néel character of the DW is stabilized by aligning the direction of the DW normal with the easy IP direction in DW tracks fabricated along the easy IP direction. Lacking the symmetry breaking of iDMI, this system exhibits bistability of Néel DWs with either chirality, and enables the chirality to be switched with an IP magnetic field. We show that the two stable chiralities are separated by an energy barrier that is large compared to the thermal energy, which allows the chirality to encode information in a nonvolatile manner. We further show that chirality switching occurs through the nucleation and propagation of Bloch lines (BLs), whose nucleation energy we extract for the first time by measuring the dependence of the chirality reversal on the magnitude and timescale of magnetic field pulses. We investigate the flow regime of SOT-driven motion of the IP anisotropy-stabilized Néel DWs, which exhibits a non-monotonic dependence on current density as a result of the competition between the effective fields from SOT and IP anisotropy, and we further explore the potential implementation of random number generation based on DW chirality switching. This scheme provides a new degree of freedom to individually program the chirality and direction of motion of DWs in a racetrack, opening up novel possibilities for spintronic device designs.

Results

A EuG film with a thickness of 12 nm was epitaxially grown on a (110)-oriented gadolinium gallium garnet (GGG) substrate using pulsed laser deposition. The film is perpendicularly magnetized (lowest energy axis normal to the film plane and remanent magnetization oriented out-of-plane (OOP) [110]) due to a dominant magnetoelastic anisotropy resulting from the lattice mismatch between the GGG substrate (lattice parameter 12.376 Å) and the EuG film (12.498 Å)¹¹ combined with positive magnetostriction coefficients λ_{111} and λ_{100} . In addition, the reduced IP symmetry compared to more common (111)-oriented garnet films results in a uniaxial anisotropy within the film plane¹², with the IP lowest energy axis oriented along $\bar{[110]}$ (defined as the \hat{x} -axis). The anisotropy landscape is hence biaxial and can be parameterized as $K(\theta, \phi) = K_{u, OOP}^{\text{eff}} \sin^2 \theta \cos^2 \phi + K_{u, IP} \sin^2 \theta \sin^2 \phi$, where θ is the polar angle measured from $\bar{[110]}$ (defined as the \hat{z} -axis) and ϕ the azimuthal angle measured from the $\bar{[110]}$ axis. Here, the OOP anisotropy, $K_{u, OOP}^{\text{eff}}$, defines the effective anisotropy within the \hat{x} - \hat{z} plane normal to the film plane, including demagnetizing effects, and $K_{u, IP}$ corresponds to anisotropy within the \hat{x} - \hat{y} film plane.

To quantify $K_{u, OOP}^{\text{eff}}$ and $K_{u, IP}$, we performed spin-Hall magnetoresistance (SMR) measurements¹³ on a patterned EuG/Pt (4 nm) Hall cross to probe the equilibrium magnetization direction as a function of applied field H along the principal anisotropy axes, $\bar{[110]}$, $\bar{[110]}$ and $[001]$, i.e., \hat{z} , \hat{x} , \hat{y} (Fig. 1a). The square hysteresis loop along $\bar{[110]}$ shows that the film has PMA and the difference of the IP saturation field along $\bar{[110]}$ and $[001]$ indicates the presence of an IP anisotropy. Fitting a macrospin model to the experimental data¹² and using the measured saturation magnetization $M_s = 77 \text{ emu/cm}^3$, we extracted $K_{u, OOP}^{\text{eff}} = 1.08 \times 10^5 \text{ erg/cm}^3$ (10.8 kJ/m³) and $K_{u, IP} = 1.96 \times 10^5 \text{ erg/cm}^3$ (19.6 kJ/m³), with corresponding anisotropy fields $H_{k, OOP}^{\text{eff}} = 2810 \text{ Oe}$ and $H_{k, IP} = 5100 \text{ Oe}$, respectively. The anisotropy landscape (Fig. 1b) hence favors OOP domains with DWs whose spin rotation is confined to the \hat{x} - \hat{z} plane (Fig. 1bi) due to the large anisotropy within the film plane (Fig. 1bii), evidenced by X-ray magnetic circular dichroism photoemission electron microscopy (XMCD-PEEM) measurements showing OOP domains with spins at the center of DWs aligned along the IP easy \hat{x} -axis (Supplementary). Contributions to the anisotropy landscape include magnetoelastic anisotropy ($K_{ME, OOP} \sim 4 \times 10^4 \text{ erg/cm}^3$, $K_{ME, IP} \sim 2 - 4 \times 10^5 \text{ erg/cm}^3$), magnetostatic (shape) anisotropy ($K_{MS, OOP} \sim -4 \times 10^4 \text{ erg/cm}^3$), surface anisotropy ($E_{\text{surface}, IP} \sim 8 \times 10^{-2} \text{ erg/cm}^2$, $E_{\text{surface}, OOP} \sim 3 \times 10^{-3} \text{ erg/cm}^2$), and magnetocrystalline anisotropy ($K_1 \sim -3.8 \times 10^4 \text{ erg/cm}^3$)¹².

cm^2 , $E_{\text{surface}, OOP} \sim 3 \times 10^{-3} \text{ erg/cm}^2$), and magnetocrystalline anisotropy ($K_1 \sim -3.8 \times 10^4 \text{ erg/cm}^3$)¹².

We utilized the IP anisotropy to stabilize Néel DWs by patterning magnetic racetracks parallel to the \hat{x} -axis, such that the IP easy axis coincides with the normal of the track-confined DW (Fig. 1c). Spins at the center of the DW are stabilized by IP anisotropy to orient parallel (blue arrow) or antiparallel (red arrow) to the IP easy axis (\hat{x} -axis). The parallel case gives rise to a clockwise (CW) up-down Néel wall and a counterclockwise (CCW) down-up Néel wall, while the antiparallel case gives rise to a CCW up-down Néel wall and a CW down-up Néel wall. Generally, an effective field exceeding the DW shape anisotropy field $H_{\text{shape}} = \frac{t \ln 2 M_s}{\pi \Delta_{\text{DW}}}$ is required to ensure fully Néel DWs¹⁴. Here, t is the film thickness, $\Delta_{\text{DW}} = \sqrt{A/K_{u, OOP}^{\text{eff}}}$ is the DW width, and A is the exchange constant. We estimate a threshold $H_{\text{shape}} = 138 \text{ Oe}$ required to stabilize Néel DWs¹⁵⁻¹⁷ (Fig. 1c), and since $H_{k, IP}$ far exceeds this threshold, we expect rigid Néel DWs in this system. The DW anisotropy, also referred to as DW stiffness, controls the SOT-driven behavior in the flow regime and is given by $H_{K, DW} = H_{k, IP} - H_{\text{shape}} = 5000 \text{ Oe}$.

Racetracks were fabricated from a EuG/Pt (4 nm) bilayer (see Methods), in which the Pt overlayer was used to generate current-induced SOT. The direction of SOT-driven DW motion depends on the DW chirality, providing a convenient means to probe the internal DW configuration. Figure 2 shows wide-field magneto-optical Kerr effect (MOKE) images of field-free current-driven DW displacement as the DW chirality was toggled using an IP magnetic field. First, a CCW DW was initialized by preparing an up-down DW and applying a field H_x^{set} along $-\hat{x}$ ("left") to set the internal orientation (see Methods). A current pulse was then applied to trigger displacement via DW creep. The SOT-driven DW motion (Fig. 2b) was antiparallel to the charge current, as expected when Pt is on top¹⁸. In Fig. 2c, d, a displacement current pulse was then injected after applying an IP field along $+\hat{x}$ ("right") and $-\hat{x}$, respectively, which toggled the direction of current-driven displacement in a manner consistent with chirality reversal. Performing the same procedure on a down-up wall gives the opposite direction of current-driven motion. We conclude that Néel DWs of either chirality are stable at equilibrium.

To quantify the DW configurational stability, we first determined the critical field $H_{x, c}^{\text{sw}}$ required for chirality switching. We adopted a measurement protocol in which we first initialized the internal moment of an up-down DW to point either "left" or "right." We then applied a field pulse H_x^{sw} with 1 s pulse width antiparallel to the DW moment, followed by a current pulse to probe the direction of current-driven displacement. For each H_x^{sw} amplitude, we repeated the sequence 100 times to determine the switching probability. In Fig. 3, the blue (red)-colored branches plot the probabilistic DW moment orientation as a function of H_x^{sw} , corresponding, to initially-"right" and "left" states, respectively. The threshold $H_{x, c}^{\text{sw}}$ to achieve 50% switching probability is symmetric within experimental uncertainty, which implies that the influence of DMI, which would prefer one chirality over the other, is negligible compared with the effect of the IP anisotropy. This finding is consistent with other works, which find negligibly small DMI effective fields in epitaxial rare-earth garnet films with thickness $>10 \text{ nm}$ ¹⁶. The non-zero DW motion velocity in the absence of DMI aligns with a recent prediction¹⁹ in systems with orthorhombic anisotropy.

The probabilistic nature of the DW chirality switching suggests a thermally activated process, which depends on both the energy barrier landscape and the timescale. In Fig. 4a, we plot a family of curves showing the chirality switching probability P^{sw} versus applied field H_x^{sw} for various field pulse widths, τ^{sw} . We observe an inverse linear relationship between $H_{x, c}^{\text{sw}}$ and $\ln \tau^{\text{sw}}$ (Fig. 4b), which is well-fitted by a phenomenological model describing activation over an intrinsic barrier E_a^0 modulated by a Zeeman energy term $\Delta E_a = p H_x^{\text{sw}}$, i.e.,

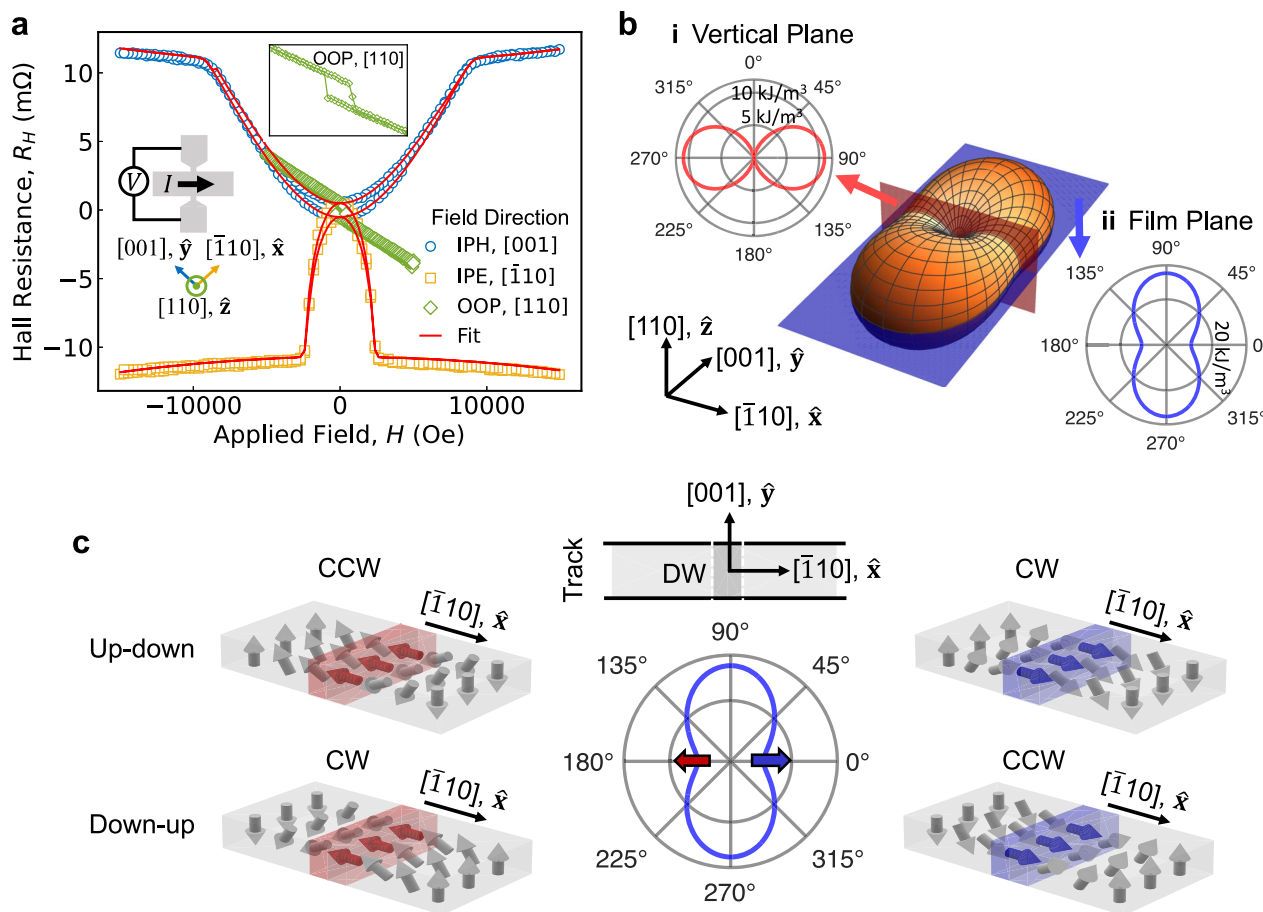


Fig. 1 | Magnetic characterization and DW structure of the film. **a** SMR data and modeled fit to extract the anisotropy energies. Transverse Hall resistances (R_H) are measured as a function of applied field (H) along IP easy (IPE), IP hard (IPH), and OOP directions, corresponding to $[\bar{1}10]$ (defined as \hat{x}), $[001]$ (defined as \hat{y}), and $[110]$ (defined as \hat{z}) directions, respectively. The square hysteresis loop (green circles) indicates that the lowest anisotropy energy axis is OOP, $[110]$, and the slope originates from the ordinary Hall effect. A zoomed-in plot of the OOP hysteresis loop with a field range of ± 2000 Oe is shown in the inset. The OOP anisotropy energy density, $K_{u,OOP}^{\text{eff}}$ is extracted from the saturation field, $H_{k,OOP}^{\text{eff}}$ of the $[\bar{1}10]$ data (yellow circles). The IP anisotropy energy density, $K_{u,IP}$ is extracted from $H_{k,IP}$, the difference between the saturation fields of the $[001]$ (blue circles) and $[\bar{1}10]$

data. The red solid curves are modeled fits to the experimental data, which give $H_{k,OOP}^{\text{eff}} = 2810$ Oe and $H_{k,IP} = 5100$ Oe. A schematic of the Hall cross device, along with the \hat{x} , \hat{y} , \hat{z} coordinate system throughout this paper, is shown in the inset.

b Surface plot of the measured anisotropy landscape. The energy density along the lowest energy axis, $[110]$, is taken as the zero reference. (i) Polar plot of the projected energy density landscape on the (001) vertical plane. (ii) Polar plot of the projected energy density landscape on the (110) film plane. **c** Schematics of DW track configuration for Néel wall stabilization and of fully Néel CCW and CW DW spin structures stabilized in the film by the strong IP anisotropy corresponding to the wall center spins oriented to the left (red arrow) and to the right (blue arrow) for up-down and down-up walls.

$\tau^{\text{sw}} = \tau_0 e^{(E_a^0 - p H_x^{\text{sw}})/kT}$. Here, τ_0 is a characteristic timescale, k is the Boltzmann constant, T is the temperature, and p is a proportionality factor. Figure 4b can therefore be understood as the phase diagram for DW chirality switching, with red (blue) shaded area well below (above) the line representing deterministic switching (unchanged orientation). The gray-shaded area around the line corresponds to the probabilistic switching regime.

More rigorously, we model P^{sw} as a function of τ^{sw} and H_x^{sw} by considering the rate of successful activation over the energy barrier, $\Gamma(H_x^{\text{sw}}) = \nu e^{-\frac{E_a(H_x^{\text{sw}})}{kT}} = \nu e^{-\frac{E_a^0}{kT} - \frac{p H_x^{\text{sw}}}{kT}}$, where ν is the attempt frequency. The IP field pulse lowers the energy barrier in proportion to H_x^{sw} , and therefore exponentially increases Γ at fixed T . The switching probability can be written $P^{\text{sw}}(\tau^{\text{sw}}, H_x^{\text{sw}}) = 1 - e^{-\tau^{\text{sw}} \Gamma(H_x^{\text{sw}})}$, which exponentially approaches unity as τ^{sw} and H_x^{sw} increase. By fitting the experimental data to the model rewritten as $\ln(-\ln(1 - P^{\text{sw}})) - \ln \tau^{\text{sw}} = \frac{p H_x^{\text{sw}}}{kT} + \ln \nu - \frac{E_a^0}{kT}$ (see Methods), we can extract E_a^0 and p . Fitting the full data set from Fig. 4a, plotted in this way (Fig. 4c), yields $\frac{p}{kT} = 0.031 \pm 0.002$ Oe $^{-1}$ and

$\ln \nu - \frac{E_a^0}{kT} = -3.01 \pm 0.42$. Approximating ν by 1 GHz^{20,21}, we estimate the intrinsic energy barrier as $E_a^0 = (23.0 \pm 0.4) kT = 0.61 \pm 0.01$ eV. Since ν varies with the effective field and damping parameters²², a range of values from 0.1 to 10 GHz can be feasible^{23–25}, which increases the uncertainty $E_a^0 = (23.5 \pm 3) kT = 0.61 \pm 0.07$ eV.

The switching threshold in Fig. 4b is much smaller than the IP anisotropy field, which suggests an incoherent (heterogeneous) reversal process within the DW in contrast to a coherent rotation. More specifically, Néel wall switching takes place through the nucleation of an opposite chirality DW segment and the subsequent propagation of BLs that are spin textures separating Néel wall segments with opposite chirality²⁶ (Fig. 5a), analogous to incoherent magnetization reversal through nucleation of domains followed by propagation of DWs²⁷. More concisely, the reversal process of these Néel walls occurs through the nucleation and propagation of BLs. BLs are shown to exist in our films using XMCD-PEEM imaging (Fig. 5b), and the propagation of BLs in rare-earth iron garnets has been reported²⁸. BLs are known to exhibit a high mobility in garnet films²⁸. Once nucleated, they readily

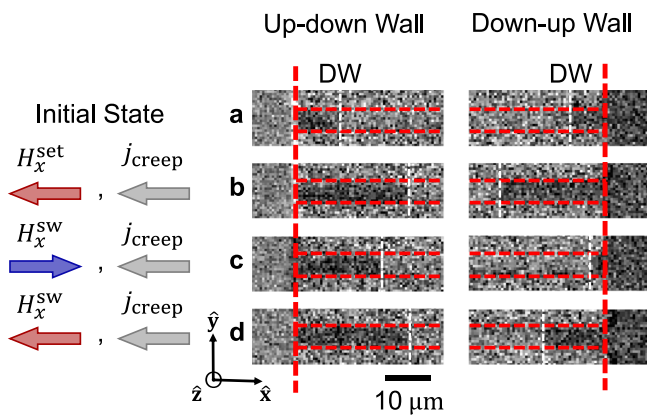


Fig. 2 | Wall chirality switching by H_x pulse. a–d Wide-field MOKE images of a DW on the racetrack whose edges are denoted by horizontal dashed lines. Dark color corresponds to an up domain and gray corresponds to a down domain. The DW positions in each frame are denoted by white dashed lines. The area to the left of the vertical red dashed line corresponds to the region covered by the contact pad and therefore does not show magnetic contrast. An up-down (down-up) wall is first initialized in the track (a). The arrows on the left of each frame denote the operation sequence of field and current pulses between the previous and the current frames. **b–d** The DW positions after the corresponding operations, which are denoted on the left of each frame. The DW moment orientation is set to the left by a H_x^{set} pulse (500 Oe, 500 ms), which results in DW motion to the right (left) for a CCW (CW) DW (a–b). The wall chirality is then switched twice by H_x^{sw} pulse (330 Oe, 1 s) to CW (CCW) and then to CCW (CW), which results in DW motion to the left (right) and then to the right (left) (b, c and c, d). The current pulse used to drive the DW is fixed at $1.33 \times 10^{11} \text{ A/m}^2$, 10 ms.

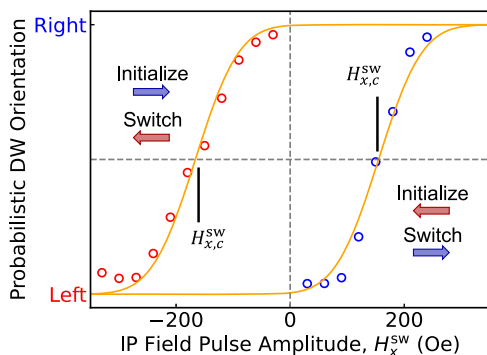


Fig. 3 | Magnetic hysteresis of a Néel DW. The probabilistic DW moment orientation is measured through DW motion as a function of the IP field pulse amplitude H_x^{sw} . The width of the H_x^{sw} pulse is 1 s. The lower (upper) range denoted by “Left” (“Right”) represents a 100% probability of measuring DW motion corresponding to a left (right)-oriented DW. On the negative H_x^{sw} branch (red circles), the DW moment orientation is initialized to the right with a 500 Oe, 500 ms IP initialization field pulse. On the positive H_x^{sw} branch (blue circles), the DW moment orientation is initialized to the left with a 500 Oe, 500 ms IP initialization field pulse. Orange solid curves are error functions fitted to the measured data, from which we obtain $H_{x,c}^{\text{sw}}$, which is the critical field amplitude, corresponding to a 50% success rate of switching the DW chirality. We extract the DW coercive field from the width of the fitted hysteresis loop, $H_{c,DW} = 160 \pm 32 \text{ Oe}$, and the DMI field from the lateral shift $H_D = 11 \pm 32 \text{ Oe}$.

propagate across the track width within the time frame of the IP field pulse, in other words, the DW chirality reversal process is nucleation-limited. Therefore, the energy barrier E_a for the reversal process corresponds to the nucleation of BLs.

To understand E_a^0 in terms of this process (Fig. 5a), consider a homogeneous Néel DW oriented to the left (red color arrows, frame A). An applied field $+H_x$ favors spins oriented to the right, which tends to

nucleate a 360° BL (i.e., a pair of 180° BLs, blue color arrows) in the DW (frame B). In the presence of H_x , the rightward-oriented region then grows rapidly, with the two 180° BLs moving away from each other (frame C). Eventually, the rightward-oriented region grows to span the entire DW, resulting in a wall that is fully Néel and oriented to the right (blue color arrows, frame D). Another possible process is that instead of nucleating a 360° BL at the center of the wall (frame B), a 180° BL nucleates at the track edge where defects and local spin misalignments exist. Both processes are feasible. While edge nucleation is energetically favored, center nucleation is statistically favored by a factor given by the center-to-edge area ratio of $\frac{w}{\Delta_{DW}} \sim 10^3$, where w is the track width.

We schematically consider the potential energy landscape for process A \rightarrow D in Fig. 5c. State B represents an intermediate state with maximum energy. The energy barrier is denoted by E_a . With no applied field, A_0 and D_0 are degenerate in energy, and the energy barrier (the difference between state A_0 and state B_0) is E_a^0 , representing the exchange and anisotropy energy penalty imposed by forming a 360° BL. With finite H_x favoring a DW with internal spins oriented to the right, the Zeeman term lifts the energy for state A and lowers the energy for state D by the same amount, δ , creating a driving force for DW chirality switching A \rightarrow D. The Zeeman term raises the energy for state A more than state B, effectively lowering the energy barrier by $\Delta E_a = -\mu_0 M_S \int_{DW} (\mathbf{m}_A - \mathbf{m}_B) \cdot \mathbf{H}_x dV \approx \ln(1 + e^{d_{BL}/\Delta_{BL}}) \pi t \Delta_{DW} \Delta_{BL} \mu_0 M_S H_x$ (see Methods), where Δ_{BL} is the 180° BL width, d_{BL} is the distance between the nucleated BLs (length of the nucleated DW segment) and the integration is over the DW volume. The lowering of the energy barrier is $\Delta E_a \propto H_x$, with the proportionality factor $p \approx \ln(1 + e^{d_{BL}/\Delta_{BL}}) \pi t \Delta_{DW} \Delta_{BL} \mu_0 M_S$. The equilibrium BL width is given by $\Delta_{BL} = \sqrt{\frac{A}{K_{eff,IP} - H_{shape} M_S/2}} = 14.8 \text{ nm}^{26}$. Using the fitted value for p obtained above, we estimate $d_{BL} = 18.5 \text{ nm}$, which is on the order of the exchange length. For edge nucleation, the proportionality factor changes to $p \approx \ln(1 + e^{2d_{BL}/\Delta_{BL}}) \frac{\pi}{2} t \Delta_{DW} \Delta_{BL} \mu_0 M_S$, which gives $d_{BL} = 21.9 \text{ nm}$. The assumption of center or edge nucleation does not affect the qualitative phenomena but only leads to quantitative modifications to the extracted nucleation length.

Néel walls stabilized by IP anisotropy behave differently from Néel walls stabilized by DMI in their current-driven motion in the flow regime because of the functionally different torques applied to the DW. Figure 6a shows the linear motion of the DW under a nanosecond current pulse from which the DW velocity v is extracted. We investigate the SOT-driven dynamics by studying the dependence of the DW motion velocity on IP field H_x (Fig. 6b) and current density j (Fig. 6c). While the effective field from DMI is unidirectional, the IP anisotropy field is uniaxial. DMI stabilizes one chirality of DW, with the chirality determined by the sign of DMI, and it acts to introduce a horizontal shift of the v curves such that the velocity is non-zero at zero field^{7,9}. IP anisotropy field stabilizes both CW and CCW chiralities. Therefore, at an IP field greater than the wall chirality switching field, the DW motion direction is determined by the IP field polarity and positive and negative IP fields increase the DW velocity symmetrically (Fig. 6b). DW velocity shows a non-monotonic dependence on the current density j (Fig. 6c). Above a depinning threshold current density of $j_0 = 2 \times 10^{11} \text{ A/m}^2$, the DW velocity firstly increases linearly with current density with a mobility $\mu = \frac{v}{j-j_0} = \frac{\pi \Delta_{DW} M_S \chi}{2 \alpha_{eff} \delta S} = 50 (\text{m/s}) / (10^{11} \text{ A/m}^2)$. As current density continues to increase, the DW velocity deviates from the linear dependence, reaching a peak at $7 \times 10^{11} \text{ A/m}^2$, beyond which increasing current density decreases the DW velocity.

The current density dependence of DW velocity can be well described by a 1D DW model^{29,30} (see Methods) as shown by the modeled fit plotted in red (Fig. 6c, d). The Néel component is represented by $\cos \psi$, where ψ is the DW internal magnetization angle. $\psi = 0^\circ$ corresponds to a pure Néel wall and $\psi = 90^\circ$ corresponds to a pure

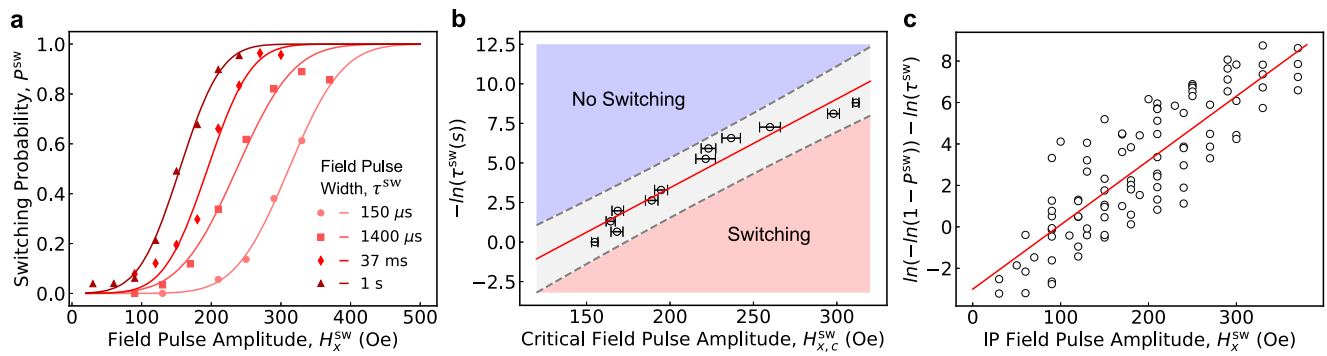


Fig. 4 | Wall chirality switching behavior and its dependence on IP field pulse width and amplitude. **a** Example line scans of the probability of successfully switching the wall chirality, P^{sw} , as a function of the switch pulse amplitude H_x^{sw} at different pulse widths τ^{sw} . With the DW initialized to be CCW for an up-down wall, an IP field pulse with pulse width τ^{sw} and pulse amplitude H_x^{sw} is applied to switch the DW to CW. Solid lines are error functions fitted to the experimental data. **b** Phase diagram for wall chirality switching. $\ln(\tau^{\text{sw}}(s))$ is plotted against the threshold pulse amplitude, $H_{x,c}^{\text{sw}}$ which are extracted from the error function fit to

each line scan. Error bars plotted are obtained from the fit. The red solid line is a linear fit to the plotted data, showing the negative correlation between pulse amplitude and width required for switching the DW chirality. In the red (blue) colored region, switching (not switching) events occur deterministically. In the gray-colored region, switching occurs probabilistically. **c** Global fitting using the expression $\ln(-\ln(1 - P^{\text{sw}})) - \ln \tau^{\text{sw}} = \frac{pH_x^{\text{sw}}}{kT} + \ln \nu - \frac{E_a^0}{kT}$ to extract the energy barrier for DW chirality switching, E_a^0 and the lowering of the energy barrier by the applied IP field, pH_x^{sw} .

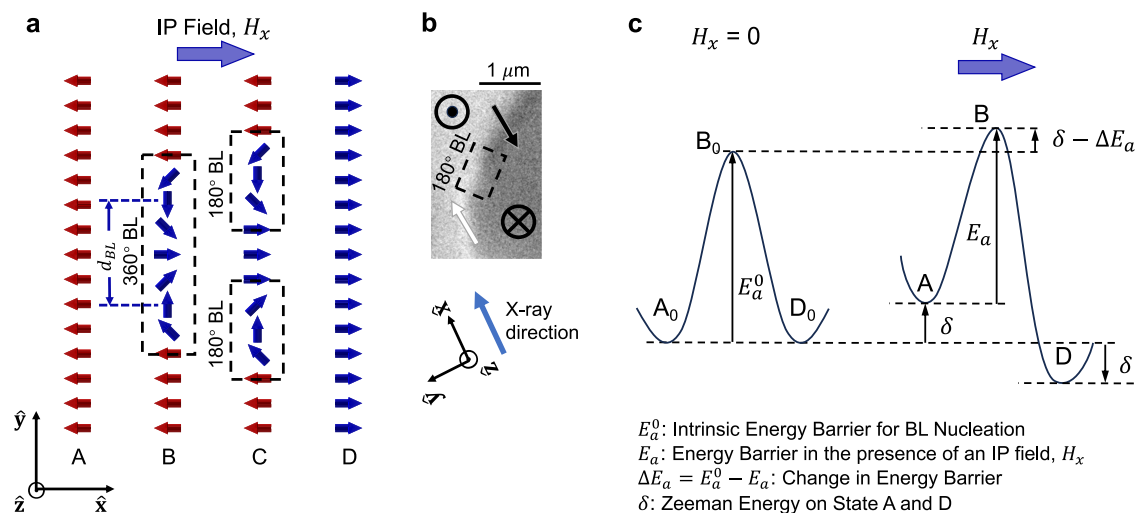


Fig. 5 | Néel wall chirality switching by BL nucleation and propagation. **a** Schematic illustration of the wall chirality switching process (top view) under the IP field H_x . A, Initial state of a purely Néel wall oriented to the left. B, The wall with a BL nucleated under the driving force H_x . C, The switched region (blue) grown under H_x by BL propagation. D, The wall becomes fully Néel to the right after the switched region expands across the entire wall. **b** An XMCD-PEEM image of two DWs with opposite spin orientations intersecting, where a 180° BL exists to maintain spin continuity. The spin orientation at the center of the DW is indicated by

arrows. X-ray direction is aligned with the IP easy axis such that spin orientation at the center of DW gives maximum contrast (white contrast for parallel and dark contrast for antiparallel with the IP easy axis). The film image is 37 nm in thickness with a similar anisotropy landscape. Details of imaging conditions are discussed in the Supplementary. **c** Potential energy landscape for the BL nucleation process (A \rightarrow D). The driving force from H_x is denoted by 2δ . The energy barrier is denoted by E_a , and the lowering of the energy barrier by H_x is denoted by ΔE_a .

Bloch wall. The SOT-driven motion is most efficient for a Néel wall. The equilibrium DW angle ψ is determined by the competition between the effective field from the current-induced SOT, which favors the Bloch character and the IP anisotropy field, which acts as a stiffening field to favor the Néel character. Application of the IP field H_x increases the DW velocity as it strengthens the IP anisotropy field to increase the DW Néel component (Fig. 6b).

To understand the dynamics, we consider the DW velocity (Fig. 6c) and DW character (Fig. 6d) at different current densities. The linear component at low current densities corresponds to the DW being largely Néel. In the limit of an infinitely large IP anisotropy field ($H_{k,\text{IP}} \rightarrow \infty$), the DW stays Néel independent of current density, and the velocity vs. current density remains linear. In our case, where the $H_{k,\text{IP}}$ is finite, the SOT effective field dominates at high current densities, and the velocity decreases with current density as the DW gains an increasingly Bloch

character. The deviation of experimental data from the analytical model at high current densities (above the peak velocity) is a result of a transient behavior as the current changes the DW character, as illustrated in previously reported micromagnetic simulations²⁹. As shown by the dashed plot for a typical DMI field of $H_D = 50\text{Oe}$ ^{4,15,16} in the absence of an IP anisotropy, the presence of an IP anisotropy increases the DW peak DW velocity by ten times because of the smaller DW canting at current densities below $8.5 \times 10^{11}\text{A/m}^2$.

The peak velocity corresponds to a DW angle of $\psi = 45^\circ$ (Fig. 6c, d) because the internal torque on the DW is maximized at this angle. Further increase in current density leads to a decline in velocity until the velocity reaches zero when the DW becomes fully Bloch. As shown in Eq. M4, the peak velocity is determined by the DW stiffness ($H_{k,\text{DW}}$) and width (Δ_{DW}) and the effective gyromagnetic ratio ($\gamma_{\text{eff}} = \frac{M_s}{\delta S}$), and the corresponding current density is determined by the effective

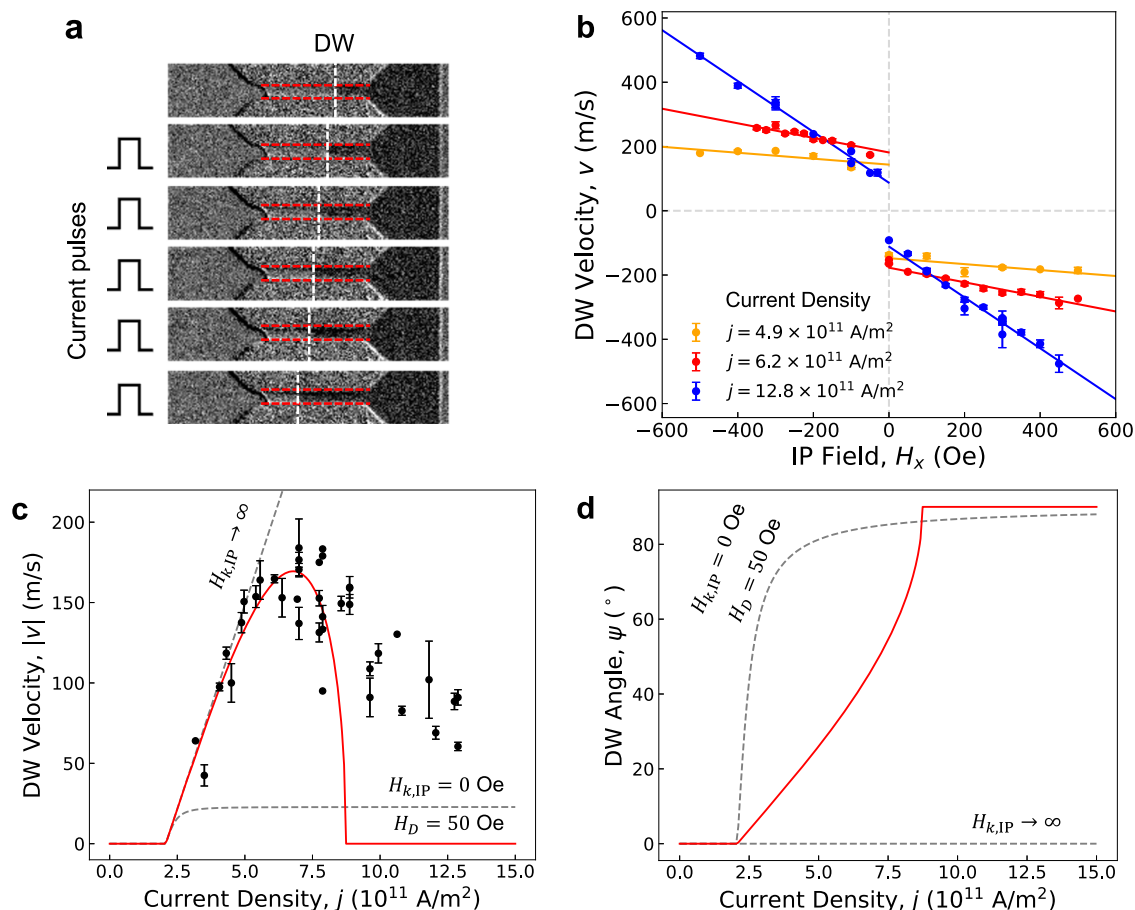


Fig. 6 | SOT-driven motion of DW stabilized by IP anisotropy. a Example of sequential images of the DW position captured after applying a current pulse between each frame (with pulse width 12 ns and pulse amplitude $9.2 \times 10^{11} \text{ A/m}^2$) without an external field. **b** DW velocity v plotted as a function of the IP field H_x for three selected current densities, corresponding to the low ($4.9 \times 10^{11} \text{ A/m}^2$), intermediate ($6.2 \times 10^{11} \text{ A/m}^2$), and high ($12.8 \times 10^{11} \text{ A/m}^2$) current density regime, respectively. Error bars in DW velocity are obtained from the linear fit of DW displacement to pulse number. **c** DW velocity v plotted as a function of the current

density under zero field. Experimental data points are plotted as black circles, and the solid red curve represents the fit to the analytical 1D DW model (see Methods). Dashed gray plots represent the analytical model with the two limiting cases of infinitely large IP anisotropy field ($H_{k,IP} \rightarrow \infty$) and a 50 Oe DMI field with zero IP anisotropy field ($H_{k,IP} = 0 \text{ Oe}$, $H_D = 50 \text{ Oe}$), while other parameters are kept the same as the fit. **d** Calculated DW internal magnetization angle ψ from the analytical models for the fit (red), the two limiting cases $H_{k,IP} \rightarrow \infty$ and $H_{k,IP} = 0 \text{ Oe}$, $H_D = 50 \text{ Oe}$ (dashed gray).

damping (α_{eff}) and the spin-Hall efficiency (χ_0) as discussed in the Supplementary. The peak velocity can therefore be further increased by tuning the anisotropy landscape, specifically, increasing the DW stiffness and decreasing the PMA strength (to increase DW width) through tuning temperature and film thickness³¹, or increasing the effective gyromagnetic ratio by tuning rare-earth composition or temperature to near angular momentum compensation ($\delta S = 0$).

Discussion

The extracted energy barrier $E_a^0 = (23.5 \pm 3)kT = 0.61 \pm 0.07 \text{ eV}$ for Néel wall chirality reversal is significantly larger than the thermal excitation at room temperature, making pure Néel walls (left- or right-oriented) thermodynamically stable states at room temperature. The energy barrier can be increased further through materials optimization, such as increasing the IP anisotropy via the film thickness and composition^{12,32}. The bistability of the two DW states, together with the nanometer length scale of DWs, suggests the possibility of high-density nonvolatile memory storage, where the binary bits can be encoded as the wall chiralities. Local fields such as the Oersted field of a thin current-carrying line⁵, for instance, can be used to individually program the wall polarity. Read-out of the DW chirality can be carried out either through a magnetic tunnel junction (MTJ) with an IP fixed layer^{33,34}, or through the direction of the current-driven DW motion

illustrated in this work. While the insulating nature of EuIG makes it MTJ integration challenging, possible schemes to incorporate MTJ readout could include exchange coupling^{35–37} the magnetization in garnet with a conductive metallic ferromagnet free layer or increasing garnet conductivity through doping^{38,39}. Engineering similar anisotropy landscapes in metallic ferromagnets is also an important pathway to generalize the bistable Néel walls demonstrated in this work through controlled deposition^{40,41} or nanofabrication^{42,43} to introduce IP anisotropy.

In addition, probabilistic computing⁴⁴ can be potentially implemented using the thermally assisted energy barrier-crossing process to switch between DW chirality states. As an example, using n walls initialized to the left and a pair of ($H_{x,c}^{\text{SW}}$, τ^{SW}) parameters corresponding to a 50% success rate, random number generation from 1 to 2^n can be generated and stored as nonvolatile bits. We present a proof-of-principle demonstration of a two-bit random number generator using two parallel tracks on a multiwire device (Fig. 7). The switching of DW chirality, which is read out through the current-driven DW motion direction, is encoded as 0 and 1. As shown in the frames in Fig. 7a, which are obtained by taking the difference between the images before and after the current injection, the black and white boxed regions represent a successful switch (1) and an unsuccessful switch (0) of the DW chirality. With the postselection of events corresponding to a ~50%

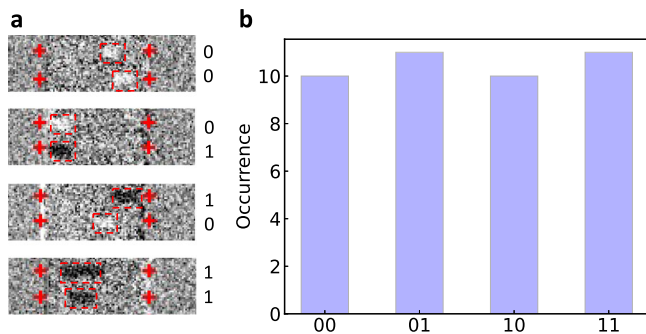


Fig. 7 | Demonstration of a two-bit random number generator. **a** Examples of two-bit states represented by the DW motion direction on two DW tracks. Each image is obtained from the difference between the image taken before and after a creep current pulse. The red crosses mark the horizontal and vertical position of a DW track. Black in the boxed area represents a successful switching of DW chirality by H_x^{sw} encoded as 1, whereas white indicates that the DW chirality remains the same as that set by the field pulse, H_x^{set} , encoded as 0. The four images shown therefore represent 00, 01, 10, and 11, respectively, as labeled next to each image. **b** Histogram for each two-bit state.

success rate on each track, we generate a histogram of the occurrence of the four possible states, 00, 01, 10, and 11, shown in Fig. 7b. The probability of observing each state is equal, which demonstrates the feasibility of random number generation using the proposed scheme. With further automation and optimization of multiwire devices, this can be easily scaled to larger bit numbers.

BLs, for which the nucleation and propagation are critical to the thermally activated DW chirality reversal described in this work, have been investigated for their potential applications as memory storage bits in the context of vertical Bloch lines (VBLs)⁴⁵. Other scientifically interesting possibilities for BLs have also been proposed, such as topologically protected DW skyrmions in the form of BLs in systems with DMI⁴⁶, and BLs in antiferromagnets with IP anisotropy as analogs of fluxon states in Josephson junctions⁴⁷. The BL width (~10 nm) and energy (~10 kT) from micromagnetic simulations reported in the literature (at zero DMI)⁴⁶ also agree with the order of magnitude estimated in this work.

In conclusion, the demonstration of bistable DW chirality states in a perpendicularly magnetized thin film with an IP anisotropy, as well as their controlled reversal using IP field pulses and readout using current pulses, could inspire many future spintronic devices, such as DW chirality-based logic and storage devices, probabilistic computing devices, etc. The study of the DW reversal statistics also allows for the extraction of BL parameters, which are of scientific importance but are difficult to directly probe because of the nanometer size of BLs.

Methods

Materials growth and characterization

The 12 nm EuIG thin film was grown on a GGG (110) substrate (MTI Corporation) by pulsed laser deposition with a Compex Pro 248 nm wavelength KrF excimer laser operated at an energy of 350 mJ and a repetition rate of 10 Hz. The target used was a commercially available EuIG target (Furuuchi) with a 99.99% elemental purity. The deposition was performed at a substrate heater temperature setpoint of 900 °C, which corresponds to 700 °C at the substrate and an O₂ pressure of 150 mTorr with a chamber base pressure of 5×10^{-6} Torr. The film thickness and strain state were determined by fitting to data from high-resolution X-ray diffraction (HRXRD) measurements of the (440) reflection on a Bruker D8 HRXRD instrument. The saturation magnetization was determined to be 77 ± 8 kA/m from vibrating sample magnetometry measurements (VSM) on a thickness series of EuIG films from 5 to 50 nm grown under the same conditions.

Device patterning

About 4 nm Pt was sputtered on EuIG(12 nm)/GGG(110) from a 1-inch Pt target using a d.c. sputter system with an Ar pressure of 3 mTorr and a base pressure of 5×10^{-8} Torr. Hall crosses with a typical active area dimension of $100 \times 100 \mu\text{m}$ were patterned with standard photolithography and ion milling. The current arm of the device was aligned to 45 degrees from the IP principal anisotropy axes to maximize the IP signal. DW motion tracks were patterned using electron beam lithography and ion milling to minimize line edge roughness. DW tracks were patterned parallel to the IP easy axis for the DW to have a Néel character stabilized by IP anisotropy. A multiwire design with ten parallel $5 \times 50 \mu\text{m}$ tracks on a single device was used to acquire more statistics during a single measurement. Second-layer Ta (6)/Au (150) contacts were patterned to enhance current density uniformity and wire-bonding repeatability via lift-off.

SMR measurements

SMR measurements shown in Fig. 1a were performed at room temperature on a custom-built transport measurement setup. The current was applied through an SR830 lock-in amplifier at a frequency of 9.973 kHz and a voltage amplitude of 5 V. Device resistance was typically 100 Ω . A 10 k Ω resistor was connected in series to provide a stable current source of 0.5 mA. The transverse voltage was differentially fed back to the lock-in amplifier. The Hall magnetoresistance, R_H can be expressed in Eq. 1, where $\phi_I = 45^\circ$, R_{SMR} and $R_{\text{SMR,AHE}}$ are the changes in R_H as a function of the IP and OOP magnetization components, respectively, arising from the SMR effect, and R_{OHE} is the magnetoresistance from the ordinary Hall effect.

$$R_H = R_{\text{SMR,AHE}} \cos \theta + R_{\text{SMR}} \sin^2 \theta \sin 2(\phi - \phi_I) + R_{\text{OHE}} \mu_0 H_3 \quad (1)$$

Wide-field MOKE measurements

The sample magnetization was probed using the polar MOKE, with the Kerr rotation and ellipticity revealing the local magnetization. The measurements were performed on our custom-built, 3-axis wide-field Kerr microscope with independent OOP and IP magnetic field control. Kohler illumination was used with a 10 \times objective. The light source was a 456.6 nm wavelength LED.

All experiments are performed on 5- μm -wide racetracks. An up-down DW was first initialized on the track. A field pulse H_x^{set} of 500 Oe, 500 ms is applied along the track, sufficient to orient the DW moment parallel to the field direction. A subsequent field pulse of pulse height H_x^{sw} and pulse width τ^{sw} is then applied in the opposite direction to toggle the DW moment orientation. Pulse amplitude is varied within a range from 0 to 370 Oe and pulse width from 150 μs to 1 s. A creep current pulse of 1.33×10^{11} A/m², 10 ms is subsequently applied to drive the DW, and the resulting wall position is recorded. The wall chirality is inferred from the wall motion direction to determine whether the field pulse (H_x^{sw} , τ^{sw}) has successfully toggled the wall chirality. Each probability data point is calculated from approximately 100 repeats of the abovementioned sequence.

Variations in the absolute value of the DW displacement for different pulses are attributed to the creep nature of the DW motion. In the creep regime, the wall dynamics are strongly affected by disorder and pinning and are therefore not expected to be fully deterministic or reproducible. We have chosen to use a low current in the creep regime to probe the DW chirality because the current itself will not disturb the wall configuration, whereas fast DW motion in the flow regime might lead to a canting of wall moments. The lower current also leads to much less Joule heating, which agrees with our assumption of room temperature in the DW chirality switching process. For a 10- μm -wide track, we estimated a temperature rise of 30 K at 1.33×10^{11} A/m² and 70 K at 2×10^{11} A/m² by measuring the longitudinal resistance.

DW motion velocity measurements are performed using a custom-built nanosecond pulse generation setup. For each velocity measurement, 10 consecutive current pulses of 12 ns in duration are applied, and the wall position before and after each pulse is obtained by fitting to the DW profile function. The velocity is extracted from a linear fit of the wall displacement and pulse number.

IP field pulse generation

IP field pulses with pulse width between 150 μ s and 5.2 ms were produced with a custom-built air coil electromagnet with an inductance of 130 μ H. A current limiting resistor of 5 k Ω is connected in series, giving a rise time of 72 μ s. For pulse widths between 37 ms and 1 s, a commercial GMW electromagnet with field feedback was used to produce the IP field pulses. With the iron core removed, the field rise rate is 20 Oe/ms. The applied field is calibrated with a Gauss meter placed near the sample position.

Model for DW chirality switching through thermally activated barrier crossing

We consider the rate of BL nucleation using standard nucleation theory.

The frequency of successful attempts is $\Gamma(H_x^{SW}) = \nu e^{-\frac{E_a(H_x^{SW})}{kT}} = \nu e^{-\frac{E_a^0}{kT}} e^{\frac{pH_x^{SW}}{kT}}$, where ν is the total attempt frequency which can be approximated by the precessional frequency; E_a is the nucleation energy barrier which consists of the intrinsic nucleation energy barrier of a BL, E_a^0 , and the lowering of the energy barrier by an applied field, $\Delta E_a = pH_x^{SW}$ with p the proportionality factor; k is the Boltzmann constant and T is the temperature.

The rate equation can therefore be written as $\frac{dP^{SW}}{dt} = \Gamma(1 - P^{SW})$, where P^{SW} is the probability of DW chirality switching. Here, we neglect the rate of reversing the nucleation because nucleated BLs propagate with a negligible energy barrier. With the boundary conditions $P^{SW}|_{t^{SW}=0} = 0$ and $P^{SW}|_{t^{SW}=\infty} = 1$, the DW chirality switching probability can be written as $P^{SW}(H_x^{SW}, t^{SW}) = 1 - e^{-t^{SW}\Gamma(H_x^{SW})}$, i.e., $\ln(-\ln(1 - P^{SW}) - \ln t^{SW}) = \frac{pH_x^{SW}}{kT} + \ln \nu - \frac{E_a^0}{kT}$, which is the equation used for global fitting. The gradient of LHS vs H_x^{SW} corresponds to $\frac{p}{kT}$, and the y-intercept corresponds to $\ln \nu - \frac{E_a^0}{kT}$.

Calculation of the change in nucleation energy barrier

We start with the definition of the change in nucleation energy barrier ΔE_a when an IP field is applied:

$$\Delta E_a = -\mu_0 M_s \int_{DW} (\mathbf{m}_A - \mathbf{m}_B) \cdot \mathbf{H}_x dV \quad (2)$$

The profile of an up-down wall without and with a BL can be well approximated by the Walker ansatz³¹ (the spin structure is assumed to be homogeneous along \hat{z}):

$$\theta(\hat{x}, \hat{y}) = 2 \tan^{-1} \exp(\hat{x}/\Delta_{DW}) \quad (3a)$$

$$\phi(\hat{x}, \hat{y}) = \begin{cases} \pi, & \text{state A} \\ -2 \tan^{-1} \exp(\hat{y}/\Delta_{BL}), & \text{state B} \end{cases} \quad (3b)$$

where θ is the polar angle of local magnetization orientation \mathbf{m} at position (\hat{x}, \hat{y}) and ϕ is the azimuthal angle with respect to the \hat{x} direction. The zero point of (\hat{x}, \hat{y}) is defined as the center of the DW and the center of the 180° BL. The same profile as the DW can be used to describe the BL²⁶. For the case of center nucleation, two 180° BLs are formed, separated by a distance d_{BL} . For edge nucleation, one 180° BL is formed, separated from the edge by distance d_{BL} . Integration over

the DW profile in Eq. 2 gives the following expression for ΔE_a .

$$\Delta E_a = \begin{cases} \ln\left(1 + e^{\frac{d_{BL}}{\Delta_{BL}}}\right) \pi t \Delta_{DW} \Delta_{BL} \mu_0 M_s H_x, & \text{center nucleation} \\ \ln\left(1 + e^{\frac{2d_{BL}}{\Delta_{BL}}}\right) \frac{\pi}{2} t \Delta_{DW} \Delta_{BL} \mu_0 M_s H_x, & \text{edge nucleation} \end{cases} \quad (4)$$

SOT-driven DW motion model

The DW velocity v and its azimuthal angle ψ defined from \hat{x} -axis in the $\hat{x} - \hat{y}$ plane can be determined by solving the coupled equations in Eq. 5, where $Q=1$ for up-down wall, χ_0 is the spin-torque efficiency and the DW anisotropy field $H_{K,DW} = H_{K,IP} - H_{\text{shape}}$.

$$\begin{cases} \alpha_{\text{eff}} \delta S \frac{v}{\Delta_{DW}} = -\frac{\pi}{2} Q M_s \chi_0 j \cos \psi \\ Q \delta S \frac{v}{\Delta_{DW}} = \frac{\pi}{2} M_s (H_x - Q H_D) \sin \psi + M_s H_{K,DW} \sin \psi \cos \psi \end{cases} \quad (5)$$

With the following definitions for the net spin density δS and the effective damping α_{eff} in terms of the magnetization (M_1 and M_2), gyromagnetic ratio (γ_1 and γ_2), and spin density (S_1 and S_2) on each sublattice and the intrinsic Gilbert damping α_0 .

$$\begin{cases} \delta S = \frac{M_1}{\gamma_1} - \frac{M_2}{\gamma_2} = S_1 - S_2 \\ \alpha_{\text{eff}} = \frac{\alpha_0(S_1 + S_2)}{S_1 - S_2} \end{cases} \quad (6)$$

Data availability

Data supporting the findings of this study are available within the article and its supplementary materials. All data generated in this study are provided in the Source Data file. Source data are provided with this paper.

References

- Parkin, S. S. P., Hayashi, M. & Thomas, L. Magnetic domain-wall racetrack memory. *Science* **320**, 190–194 (2008).
- Allwood, D. A. et al. Magnetic domain-wall logic. *Science* **309**, 1688–1692 (2005).
- Vélez, S. et al. High-speed domain wall racetracks in a magnetic insulator. *Nat. Commun.* **10**, 4750 (2019).
- Avci, C. O. et al. Interface-driven chiral magnetism and current-driven domain walls in insulating magnetic garnets. *Nat. Nanotechnol.* **14**, 561–566 (2019).
- Caretta, L. et al. Fast current-driven domain walls and small skyrmions in a compensated ferrimagnet. *Nat. Nanotechnol.* **13**, 1154–1160 (2018).
- Caretta, L. et al. Relativistic kinematics of a magnetic soliton. *Science* **370**, 1438–1442 (2020).
- Emori, S., Bauer, U., Ahn, S. M., Martinez, E. & Beach, G. S. D. Current-driven dynamics of chiral ferromagnetic domain walls. *Nat. Mater.* **12**, 611–616 (2013).
- Thiaville, A., Rohart, S., Jué, É, Cros, V. & Fert, A. Dynamics of Dzyaloshinskii domain walls in ultrathin magnetic films. *EPL* **100**, 57002 (2012).
- Ryu, K.-S., Thomas, L., Yang, S.-H. & Parkin, S. Chiral spin torque at magnetic domain walls. *Nat. Nanotech.* **8**, 527–533 (2013).
- Fillion, C.-E. et al. Gate-controlled skyrmion and domain wall chirality. *Nat. Commun.* **13**, 5257 (2022).
- Eschenfelder, A. H. *Magnetic Bubble Technology* Vol. 14 (Springer, 1980).
- Song, Y., Kaczmarek, A. C., Beach, G. S. D. & Ross, C. A. Engineering an easy-plane anisotropy in an epitaxial europium iron garnet (110) film. *Phys. Rev. Mater.* **7**, 084407 (2023).
- Nakayama, H. et al. Spin Hall magnetoresistance induced by a nonequilibrium proximity effect. *Phys. Rev. Lett.* **110**, 206601 (2013).

14. Franke, K. J. A., Ophus, C., Schmid, A. K. & Marrows, C. H. Switching between magnetic Bloch and Néel domain walls with anisotropy modulations. *Phys. Rev. Lett.* **127**, 127203 (2021).
15. Fakhru, T. et al. Influence of substrate on interfacial Dzyaloshinskii-Moriya interaction in epitaxial Tm₃Fe₅O₁₂ films. *Phys. Rev. B* **107**, 054421 (2023).
16. Caretta, L. et al. Interfacial Dzyaloshinskii-Moriya interaction arising from rare-earth orbital magnetism in insulating magnetic oxides. *Nat. Commun.* **11**, 1090 (2020).
17. Emori, S. et al. Spin Hall torque magnetometry of Dzyaloshinskii domain walls. *Phys. Rev. B* **90**, 184427 (2014).
18. Liu, L., Lee, O. J., Gudmundsen, T. J., Ralph, D. C. & Buhrman, R. A. Current-induced switching of perpendicularly magnetized magnetic layers using spin torque from the spin hall effect. *Phys. Rev. Lett.* **109**, 096602 (2012).
19. Thiaville, A. & Miltat, J. Spin-orbit torque-driven domain wall motion in the absence of Dzyaloshinskii-Moriya interactions. *EPL* **146**, 66001 (2024).
20. Desplat, L. & Kim, J.-V. Quantifying the thermal stability in perpendicularly magnetized ferromagnetic nanodisks with forward flux sampling. *Phys. Rev. Appl.* **14**, 064064 (2020).
21. Li, Z. & Zhang, S. Magnetization dynamics with a spin-transfer torque. *Phys. Rev. B* **68**, 024404 (2003).
22. Suzuki, Y. & Kubota, H. in *Spintronics Handbook* (CRC Press, 2019).
23. Kanai, S., Hayakawa, K., Ohno, H. & Fukami, S. Theory of relaxation time of stochastic nanomagnets. *Phys. Rev. B* **103**, 094423 (2021).
24. Wernsdorfer, W. et al. Experimental evidence of the Néel-Brown model of magnetization reversal. *Phys. Rev. Lett.* **78**, 1791–1794 (1997).
25. Suto, H. et al. Theoretical study of thermally activated magnetization switching under microwave assistance: switching paths and barrier height. *Phys. Rev. B* **91**, 094401 (2015).
26. Malozemoff, A. P. & Slonczewski, J. C. *Magnetic Domain Walls in Bubble Materials* (Academic Press, 1979).
27. Raquet, B., Mamy, R. & Ousset, J. C. Magnetization reversal dynamics in ultrathin magnetic layers. *Phys. Rev. B* **54**, 4128–4136 (1996).
28. Logginov, A. S., Nikolaev, A. V. & Dobrovitski, V. V. Direct optical observation of vertical Bloch lines propagation by in-plane field pulses. *IEEE Trans. Magn.* **29**, 2590–2592 (1993).
29. Haltz, E., Franke, K. J. A. & Marrows, C. H. Dynamics of bistable Néel domain walls under spin-orbit torque. *Phys. Rev. B* **109**, 064406 (2024).
30. Huang, S. *Structure and Dynamics of Magnetic Domain Walls in Multi-Sublattice Magnetic Oxides*. Massachusetts Institute of Technology (2024).
31. Song, Y. et al. Temperature-dependent surface anisotropy in (110) epitaxial rare earth iron garnet films. *Small* **20**, 2407381 (2024).
32. Rosenberg, E. R. et al. Magnetism and spin transport in rare-earth-rich epitaxial terbium and europium iron garnet films. *Phys. Rev. Mater.* **2**, 094405 (2018).
33. Zhao, M. et al. Electrical detection of mobile skyrmions with 100% tunneling magnetoresistance in a racetrack-like device. *npj Quantum Mater.* **9**, 1–7 (2024).
34. Annunziata, A. J. et al. Racetrack memory cell array with integrated magnetic tunnel junction readout. In *2011 International Electron Devices Meeting* 24.3.1–24.3.4 (IEEE, 2011).
35. Pashkevich, M. et al. Tunable magnetic properties in ultrathin Co/garnet heterostructures. *J. Appl. Phys.* **111**, 023913 (2012).
36. Ben Youssef, J., Castel, V., Vukadinovic, N. & Labrune, M. Spin-wave resonances in exchange-coupled permalloy/garnet bilayers. *J. Appl. Phys.* **108**, 063909 (2010).
37. Chun, Y. S. & Krishnan, K. M. Interlayer perpendicular domain coupling between thin Fe films and garnet single-crystal underlayers. *J. Appl. Phys.* **95**, 6858–6860 (2004).
38. Zhang, Z. et al. Studies on effect of Ca-doping on structure and electrochemical properties of garnet-type Y₃-xCaxFe₅O₁₂-δ. *J. Solid State Chem.* **290**, 121530 (2020).
39. Antonini, B., Paoletti, A., Paroli, P., Scarinci, F. & Tucciarone, A. High conductivity n-type yttrium iron garnet. *J. Magn. Magn. Mater.* **31–34**, 149–150 (1983).
40. Scheibler, S., Yildirim, O., Herrmann, I. K. & Hug, H. J. Inducing in-plane uniaxial magnetic anisotropies in amorphous CoFeB thin films. *J. Magn. Magn. Mater.* **585**, 171015 (2023).
41. Li, Q. et al. Tailoring the in-plane magnetic anisotropy and permeability spectra of obliquely deposited Fe₄₀Co₄₀B₂₀ films for 5G communications. *J. Magn. Magn. Mater.* **578**, 170811 (2023).
42. Zhan, Q., Vandezande, S., Van Haesendonck, C. & Temst, K. Manipulation of in-plane uniaxial anisotropy in Fe/MgO(001) films by ion sputtering. *Appl. Phys. Lett.* **91**, 122510 (2007).
43. Paz, E., Cebollada, F., Palomares, F. J., García-Sánchez, F. & González, J. M. Control of magnetization reversal by combining shape and magnetocrystalline anisotropy in epitaxial Fe planar nanowires. *Nanotechnology* **21**, 255301 (2010).
44. Chowdhury, S. et al. A full-stack view of probabilistic computing with p-bits: devices, architectures, and algorithms. *IEEE J. Explor. Solid-State Comput. Devices Circuits* **9**, 1–11 (2023).
45. Humphrey, F. & Wu, J. Vertical bloch line memory. *IEEE Trans. Magn.* **21**, 1762–1766 (1985).
46. Cheng, R. et al. Magnetic domain wall skyrmions. *Phys. Rev. B* **99**, 184412 (2019).
47. Ovcharov, R. V., Ivanov, B. A., Åkerman, J. & Khymyn, R. S. Anti-ferromagnetic Bloch line driven by spin current as room-temperature analogue of a fluxon in a long Josephson junction. *Phys. Rev. Appl.* **20**, 034060 (2023).

Acknowledgements

The authors gratefully acknowledge support from NSF ECCS 2232830 and DMR 2323132. Y.S. was supported by a Chyn Duoq Shiah Fellowship. The authors gratefully acknowledge Allison Kaczmarek, Eunsoo Cho, Paul Fourmont, Thanh Nguyen, and Professor Mingda Li for their assistance with the beamline measurement. The authors acknowledge Brian Neltner of MIT DMSE Undergraduate Teaching Lab for his support in the Labview program development. Characterization was performed in part in the MIT Materials Research Laboratory shared facilities supported by the MRSEC Program DMR 1419807. Nanofabrication was performed at MIT.nano Facilities. This research used resources of the Center for Functional Nanomaterials and the National Synchrotron Light Source II, which are US Department of Energy (DOE) Office of Science facilities at Brookhaven National Laboratory, under Contract No. DE-SC0012704.

Author contributions

Y.S. and S.H. contributed equally to this work. Y.S., S.H., G.S.D.B., and C.A.R. conceived the project; Y.S. and S.H. planned and conducted the experiments; Y.S. prepared the samples and fabricated devices; D.B., Y.S., and S.H. developed equipment for field pulse generation; J.T.S. collected XMCD-PEEM images. Y.S., S.H., G.S.D.B., and C.A.R. analyzed the data and wrote the manuscript; all authors contributed to the discussion of the data in the manuscript.

Competing interests

The authors declare no competing interests.

Additional information

Supplementary information The online version contains supplementary material available at <https://doi.org/10.1038/s41467-025-60412-1>.

Correspondence and requests for materials should be addressed to Caroline A. Ross or Geoffrey S. D. Beach.

Peer review information *Nature Communications* thanks Rajasekhar Medapalli, Paul Noel and the other, anonymous, reviewer(s) for their contribution to the peer review of this work. A peer review file is available.

Reprints and permissions information is available at <http://www.nature.com/reprints>

Publisher's note Springer Nature remains neutral with regard to jurisdictional claims in published maps and institutional affiliations.

Open Access This article is licensed under a Creative Commons Attribution-NonCommercial-NoDerivatives 4.0 International License, which permits any non-commercial use, sharing, distribution and reproduction in any medium or format, as long as you give appropriate credit to the original author(s) and the source, provide a link to the Creative Commons licence, and indicate if you modified the licensed material. You do not have permission under this licence to share adapted material derived from this article or parts of it. The images or other third party material in this article are included in the article's Creative Commons licence, unless indicated otherwise in a credit line to the material. If material is not included in the article's Creative Commons licence and your intended use is not permitted by statutory regulation or exceeds the permitted use, you will need to obtain permission directly from the copyright holder. To view a copy of this licence, visit <http://creativecommons.org/licenses/by-nc-nd/4.0/>.

© The Author(s) 2025